Dalton Transactions

ROYAL SOCIETY OF CHEMISTRY

PAPER

View Article Online
View Journal | View Issue

Check for updates

Cite this: *Dalton Trans.*, 2024, **53**, 15164

NIR absorbing ferrocenyl perylenediimide-based donor–acceptor chromophores†

Mohd Wazid and Rajneesh Misra *

A set of ferrocenyl-functionalized perylenediimide (PDI) compounds and their 1,1,4,4-tetracyanobuta-1,3-diene (TCBD) derivatives **1–5** were designed and synthesized using palladium-catalyzed Sonogashira cross-coupling, followed by a thermally activated [2 + 2] cycloaddition–retroelectrocyclization [CA–RE] reaction with a 1,1,2,2-tetracyanoethylene (TCNE) acceptor in good yields. The TCBD group works as an acceptor, whereas the ferrocenyl group acts as a donor at the central PDI core. The effects of varying the number of ferrocenyl and TCNE groups on the photophysical, thermal, electrochemical, and spectroelectrochemical properties were studied. The di-substituted PDI derivatives **3**, **4**, and **5** exhibit bathochromic shifts in the absorption spectra compared to **1** and **2**, attributed to the extended π-conjugation. The electrochemical analysis of derivatives **2**, **4**, and **5** shows multiple reduction waves in the low potential region due to the presence of TCBD and perylenediimide acceptor units. Spectroelectrochemical studies were performed, showing that upon applying redox potentials, the absorption spectra shifted from the visible to the near-infrared (NIR) region. Computational calculations indicate that in the HOMO, the electron density is localized on the ferrocene unit, while in the LUMO, it is distributed over the PDI–TCBD unit, indicating a strong D–A interaction.

Received 7th June 2024,
Accepted 16th August 2024

DOI: 10.1039/d4dt01661k

rsc.li/dalton

Published on 20 August 2024. Downloaded on 3/15/2026 4:50:25 AM.

Introduction

In recent years, donor–π–acceptor (D–π–A) conjugated compounds have attracted substantial scientific attention due to their application in organic field-effect transistors (OFETs), organic light-emitting diodes (OLEDs), organic photovoltaics (OPVs), and nonlinear optics (NLO).[1–7] Perylenediimide has been used in D–A systems as reported in the literature.[8–10] PDI, a π-conjugated dye that belongs to the rylene family, is composed of perylene units connected by imide groups. PDI shows structural properties, such as intense 400–600 nm absorption, good electron-accepting capability, high electron mobility, high molar extinction coefficients, large fluorescence quantum yields, and chemical robustness, making it an ideal candidate for n-type semiconductors. Expanding the π-conjugation at the bay position allows PDI dyes to fine-tune their optical properties and decreases the HOMO–LUMO energy gap. Bay-substituted D–A derivatives have been widely investigated to tune their photophysical and electrochemical properties and stabilize their low-lying LUMO energy levels.[11–22] The above properties can be easily tuned by the D–A approach, in which the electron-rich group donor (D) and the electron-deficient group acceptor (A) are connected through electron-rich alkynes such as ethynyl ferrocene. The well-developed synthetic chemistry of ferrocene has attracted much attention due to its good solubility and high chemical robustness. The unique electrochemical properties of ferrocene have been exploited in NLO, superconductors, magnetic fields, semiconductors, biosensors, sensors, and redox catalyst materials.[23–26]

1,1,2,2-Tetracyanoethylene (TCNE) is a multi-cyano-based strong electron-acceptor moiety that exhibits high thermal and chemical robustness and has a wide range of applications in organic electronics. Introducing the TCNE acceptor into the backbone of a donor–acceptor ferrocenyl PDI system tailors its photophysical and electrochemical properties. The electron-rich alkyne undergoes a catalyst-free, high-yield, and rapid cycloaddition–retroelectrocyclic ring-opening reaction [CA–RE] with TCNE, leading to the formation of donor–acceptor π-conjugated molecular systems.[27–32] Shoji, Butenschön, Diederich, Michinobu, Trolez, Nakamura, and Kato *et al.* have explored TCBD and cyclohexa-2,5-diene-1,4-diylidene-expanded TCBD-substituted derivatives as redox-active ICT chromophores for optoelectronic applications.[33–50]

In 2012, our research group reported the optical and electrochemical properties of unsymmetrical mono-substituted ferrocenyl PDIs.[51] Furthermore, in 2016, our group explored the effect of substituting one or two ferrocenyl units on the PDI core using π-spacers.[52,53] Herein, we wish to report the synthesis and characterization of ferrocenyl-functionalized

Department of Chemistry, Indian Institute of Technology Indore (M.P.), 453552, India. E-mail: rajneeshmisra@iiti.ac.in

† Electronic supplementary information (ESI) available. See DOI: https://doi.org/10.1039/d4dt01661k

This journal is © The Royal Society of Chemistry 2024

Published on 20 August 2024. Downloaded on 3/15/2026 4:50:25 AM.

PDI–TCBD donor–acceptor chromophores **1–5** (Fig. 1). The investigated chromophores showed the impact of the TCBD group on their photophysical,thermal stability, and electrochemical properties. In order to investigate the spectroelectrochemical changes of PDI derivatives, their redox potentials were applied and their absorption spectra were recorded in the near-infrared (NIR) region (Fig. 4).

Results and discussion

Synthesis

The synthesis of ethynyl-bridged ferrocenyl-functionalized **PDIs 1–5** is outlined in Scheme 1. The monobromo PDI, dibromo PDI, and ferrocene precursors were synthesized following the reported procedure.[22,52,54,55] All five PDI derivatives were synthesized using the palladium-catalyzed Sonogashira cross-coupling, followed by the [2 + 2] CA–RE reaction with TCNE. The ethynyl-bridge compounds **1** and **3** were obtained by treating **PDI-1Br** and **PDI-2Br** with 1.5 and 2.5 eq. of ferrocenyl precursor (**Fc-Ph**) in a toluene : diisopropylamine mixture (1 : 1) at 80 °C for 7 h using $Pd(PPh_3)_4$/CuI as a catalyst under an inert atmosphere in 83% and 63% yields, respectively. The TCBD-substituted compound **2** was obtained in 77% yield by reacting compound **1** with 1.1 eq. of TCNE in DCM at rt for 6 h. Compounds **4** and **5** were synthesized by treating compound **3** with 1.0 and 2.5 eq. of TCNE at rt for 3 h and 6 h in 37% and 90% yields respectively. Purification of the π-conjugated donor–acceptor PDIs **1–5** was performed by column chromatography (silica gel mesh size 100–200) using dichloromethane and hexane as solvents. The presence of 2-ethyl-hexyl alkyl chains on PDI makes the compounds readily soluble in common organic solvents, such as dichloromethane, chloroform, tetrahydrofuran, and toluene. The synthesized PDI derivatives **1–5** were fully characterized by ^{1}H NMR, ^{13}C NMR, and HRMS (MALDI-TOF) techniques (Fig. S1–S15, ESI†).

Photophysical properties

Fig. 2a shows the electronic absorption spectra of PDI and its derivatives **1–5**. The electronic absorption spectra were recorded in DCM at room temperature, and the related data are tabulated in Table 1. The perylenediimide core exhibited a distinctive vibronic pattern with an intense absorption band at 524 nm. The incorporation of ferrocenyl units on PDI increases its π-conjugation, resulting in a bathochromic shift in the absorption spectra of compounds **1** and **3**. The PDI derivatives **1–5** show absorption spectra in the range of 530–800 nm. The ferrocenyl-substituted PDI derivatives **1** and **3** show absorption bands at 533 and 558 nm, respectively, while their TCBD analogs **2**, **4**, and **5** show absorption bands at 538, 563, and 565 nm, respectively. The incorporation of TCBD into PDI results in a diminishing of the distinctive vibronic pattern of PDI. This diminishing of the PDI pattern is attributed to the charge transfer from ferrocene to the PDI–TCBD units, and it

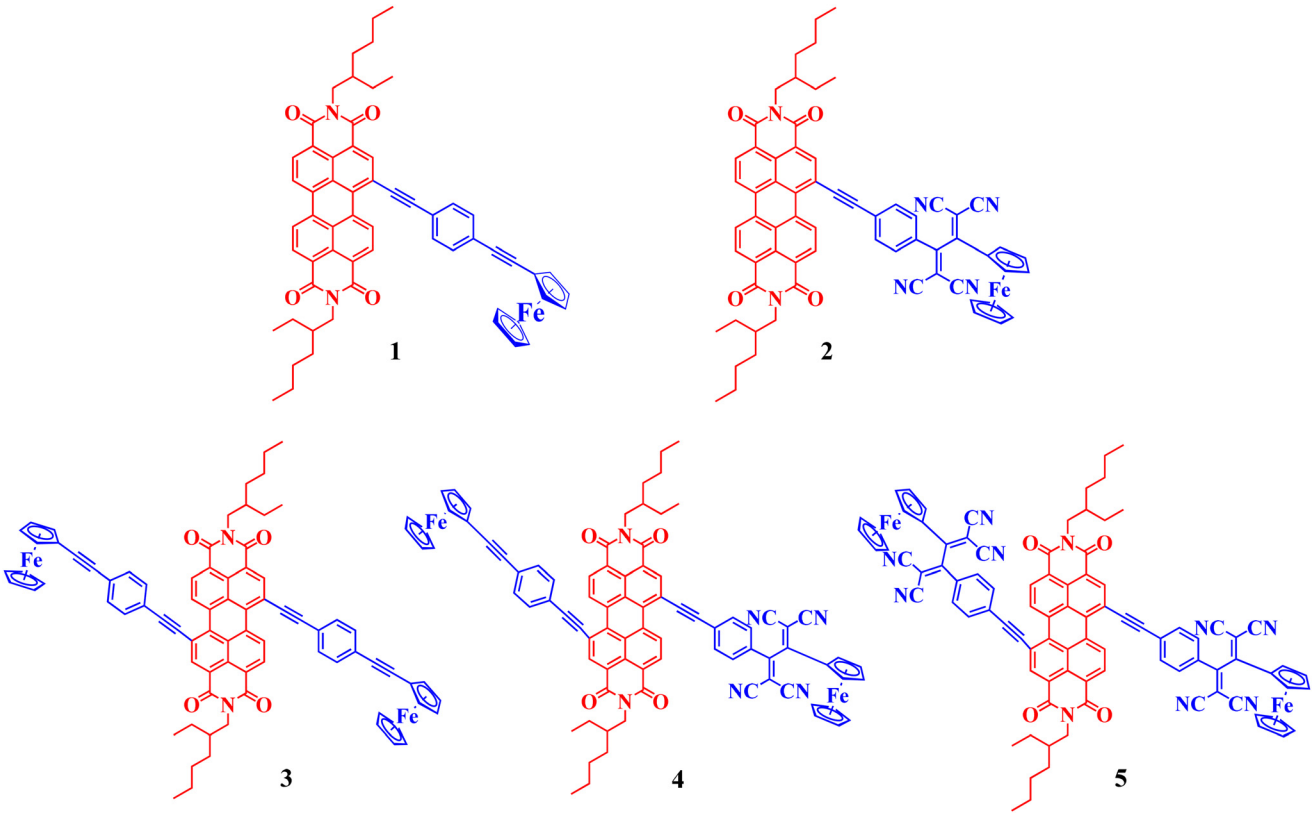

Fig. 1 Molecular structures of the PDI derivatives **1–5**.

Published on 20 August 2024. Downloaded on 3/15/2026 4:50:25 AM.

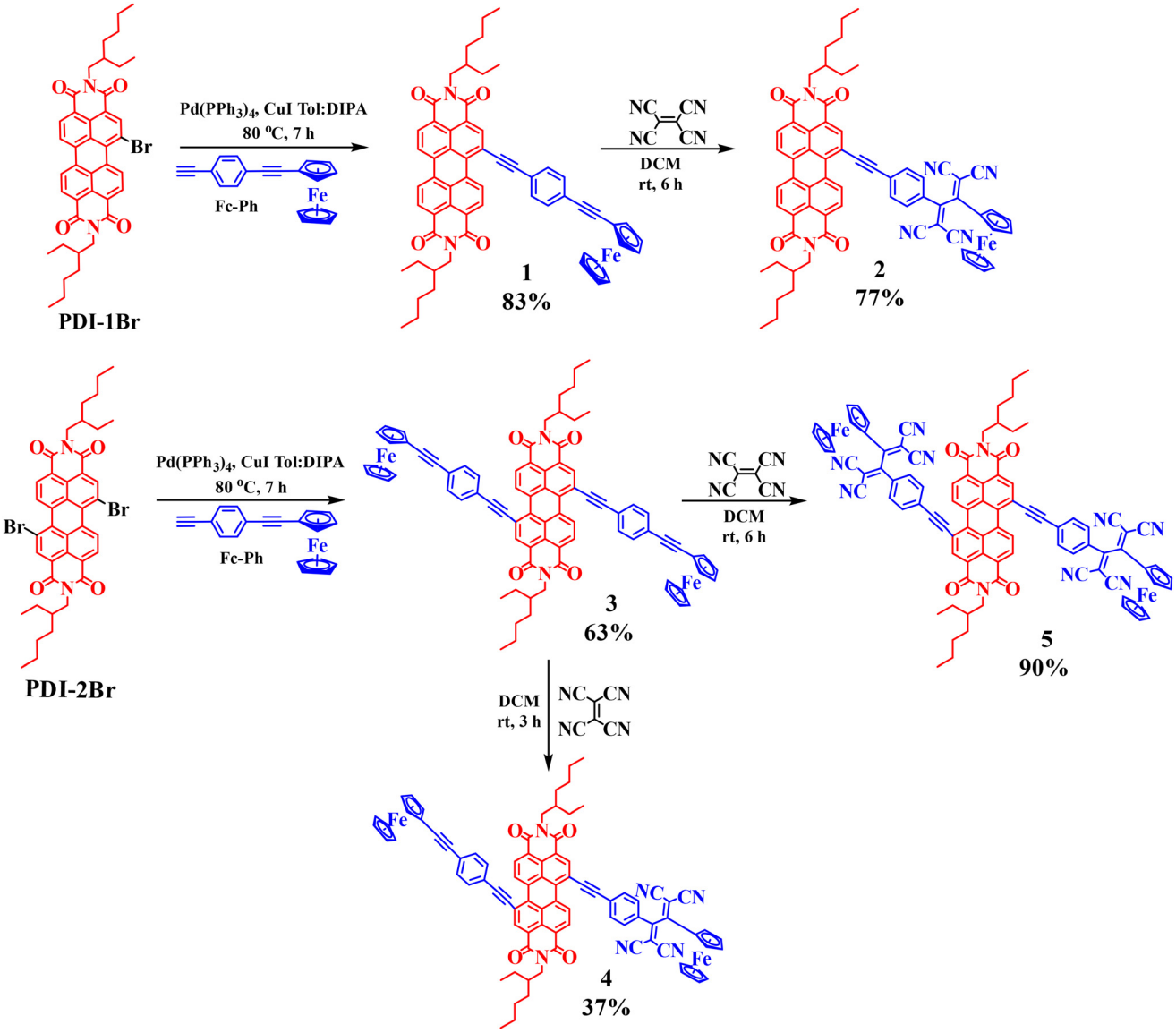

Scheme 1 Synthetic route to the donor–acceptor PDI derivatives **1–5**.

is evidenced by the appearance of a shoulder in the range of 600–800 nm.[47,48]

Solvatochromic studies of the TCBD derivatives **2**, **4**, and **5** were performed in solvents of different polarities at room temperature (Fig. S18†). The absorption spectrum of the PDI derivative **2** shifted toward a higher wavelength region, while in the case of PDI derivatives **4** and **5**, their absorption spectra showed a slight bathochromic shift. This phenomenon may arise due to the presence of charge transfer interactions within the chromophores.

Thermal stability

The thermal stabilities of the PDI derivatives **1–5** were studied by thermogravimetric analysis (TGA) in a temperature range of 50–800 °C at a heating rate of 10 °C min^{-1} under a nitrogen atmosphere. The related thermograms are depicted in Fig. 2b. The decomposition temperatures (T_d) for PDI derivatives **1–5** at 5% weight loss were recorded at 320, 408, 442, 350, and 368 °C, respectively (Table 1). The thermogram of compound **2** displays two weight loss phases between 50 and 800 °C, leaving a residual mass of around 30% at 600 °C. On the other hand, the PDI derivatives **1**, **3**, **4**, and **5** exhibit a single weight loss phase between 50 and 800 °C, leaving a residual mass of approximately 30% at 550 °C. The thermal stability of the PDI derivatives **1–5** follows the order **3** > **2** > **5** > **4** > **1**. The PDI derivative **3** shows the highest thermal stability among all the investigated compounds.

Redox properties

The electrochemical properties of the PDI derivatives **1–5** were investigated by cyclic voltammetry (CV) and differential pulse voltammetry (DPV) analyses in dry dichloromethane (DCM)

 This journal is © The Royal Society of Chemistry 2024

Published on 20 August 2024. Downloaded on 3/15/2026 4:50:25 AM.

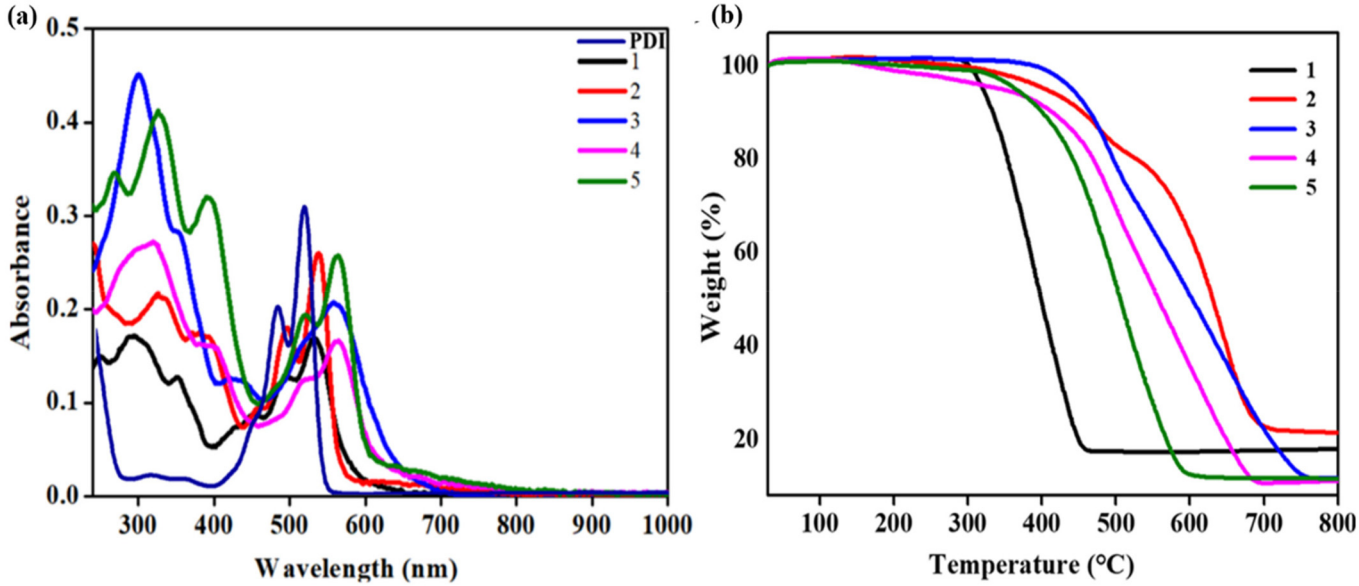

Fig. 2 (a) Absorption spectra of chromophores **1–5** and **PDI** in dry dichloromethane (1×10^{-5} M). (b) Thermogravimetric analysis of the PDI derivatives **1–5** performed at a heating rate of 10 °C min^{-1} under a nitrogen atmosphere.

Table 1 Photophysical properties of the PDI derivatives **1–5**

Compounds	λ_{max}[a] (nm)	ε[a] (M^{-1} cm^{-1})	E_g^{opt}[a] (eV)	Thermal stability[b] (T_d)
1	533	16 870	2.09	320
2	538	26 590	2.12	408
3	558	20 670	1.90	442
4	563	16 615	1.85	350
5	565	26 620	2.06	368

[a] Absorbance measured in dichloromethane at 1×10^{-5} M concentration. λ_{max}: absorption wavelength. ε: extinction coefficient. E_g^{opt}: optical bandgap. [b] Decomposition temperatures for 5% weight loss at a heating rate of 10 °C min^{-1} under an inert atmosphere.

using 0.1 M tetrabutylammonium perchlorate (TBA)ClO_4 solution as a supporting electrolyte at room temperature and Ag/AgCl as a reference electrode (Fig. 3 and S17†). The oxidation and reduction potential values were calculated from the CV plots and the peak reversibility was explained through peak potential differences ($E_{pa} - E_{pc} = \Delta E_p$/mV), where "pa" denotes the peak anodic process and "pc" denotes the peak cathodic process. Redox potentials ($E_{1/2}$) were calculated as an average of peak potentials (Table S1†). In general, the PDI moiety exhibits a two reductions potential and ferrocene exhibits a single oxidation potential.[19,49] The ferrocenyl PDI derivatives **1–3** displayed a single reversible oxidation wave within the range of 0.49–0.96 V, whereas compounds **4** and **5** showed two reversible oxidation waves in the anodic region. Derivative **1** displays a single reversible oxidation wave during anodic scanning with peak potential $E_{1/2}$ = 0.64 V and a ΔE_p of 80 mV. In addition, cathodic scanning encompasses two reversible reduction processes. The first peak potential is $E_{1/2}$ = −0.50 V with a ΔE_p of 79 mV, while the second peak potential is $E_{1/2}$ = −0.67 V with a ΔE_p of 79 mV. These oxidation and reduction processes are related to the ferrocene and PDI moieties, respectively. Derivative **2** showed a single reversible oxidation wave in the anodic region at $E_{1/2}$ = 0.96 V, corresponding to the ferrocene unit. On the other hand, there are four reversible reduction waves in the cathodic region. Among the four reduction waves, two specifically labeled as waves (i) and (ii) represent reversible peaks, corresponding to the TCBD acceptor with peak potentials of $E_{1/2}$ = −0.29 and −0.45 V, respectively; the remaining two waves, (waves iii and iv) correspond to the PDI moiety. Waves (iii) and (iv) are reversible in nature with peak potentials of $E_{1/2}$ = −0.61 V and $E_{1/2}$ = −0.83 V (ΔE_p = 30 mV), respectively. During anodic scanning, derivative **3** exhibited a reversible oxidation wave in the anodic region, which corresponds to ferrocene. The peak potential for this wave is $E_{1/2}$ = 0.64 V with a peak-to-peak potential separation of ΔE_p = 70 mV. During cathodic scanning, two reversible reduction waves (waves i and ii) were observed for the perylenediimide moiety with peak potentials of $E_{1/2}$ = −0.44 V (ΔE_p = 79 mV) and $E_{1/2}$ = −0.62 V (ΔE_p = 80 mV), respectively. The mono-TCBD compound **4** shows two reversible oxidation waves in the anodic region and their respective peak potentials are $E_{1/2}$ = 0.49 V (ΔE_p = 70 mV) and 0.83 V (ΔE_p = 80 mV), which correspond to ferrocene (first potential wave for Fc located far from TCBD) and the ferrocene moiety (second potential wave for Fc close to TCBD), respectively. The second oxidation potential wave for compound **4** is anodically shifted compared to the first oxidation potential wave due to the electron density delocalization of ferrocene over the PDI–TCBD unit. During cathodic scanning, compound **4** exhibited four reversible reduction waves, with peak potentials of $E_{1/2}$ = −0.47 and −0.57 V corresponding to the TCBD acceptor, while the remaining two reduction waves with peak potentials of $E_{1/2}$ = −0.75 V and −0.85 V are attributed to

Published on 20 August 2024. Downloaded on 3/15/2026 4:50:25 AM.

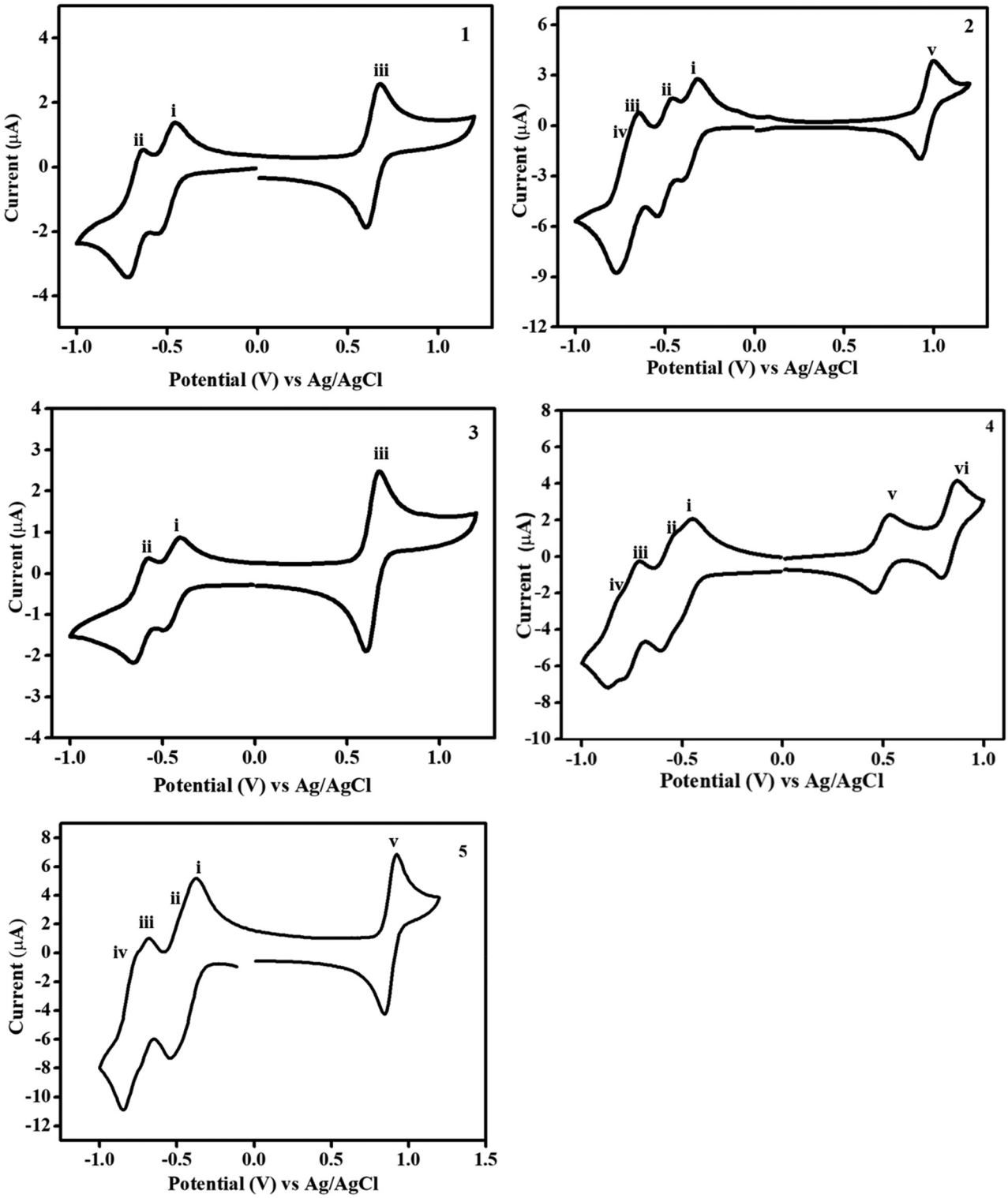

Fig. 3 Cyclic voltammograms of the donor–acceptor PDI derivatives **1–5** in a 0.1 M solution of (TBA)ClO_4 as a supporting electrolyte in dichloromethane at a 50 mV s^{-1} scan rate *versus* Ag/AgCl at 25 °C.

the PDI moiety. During cathodic scanning, compound **5** displayed four reversible reduction waves. Among these, two are reversible waves corresponding to TCBD (waves i and ii) with peak potentials of $E_{1/2}$ = −0.34 and −0.46 V, respectively. The remaining two reversible waves can be attributed to PDI (waves 3 and 4) with peak potentials of $E_{1/2}$ = −0.64 and −0.76 V. Additionally, compound **5** exhibited one oxidation wave in the anodic region for the ferrocene moiety, with a peak poten-

 This journal is © The Royal Society of Chemistry 2024

Published on 20 August 2024. Downloaded on 3/15/2026 4:50:25 AM.

tial of $E_{1/2}$ = 0.96 V and a ΔE_p of 84 mV. The oxidation potentials of ferrocene PDI derivatives **1–5** were found to be higher than that of free ferrocene, due to substantial electron delocalization from ferrocene to the acceptor PDI–TCBD.

Spectroelectrochemistry

Spectroelectrochemical analysis was carried out to investigate the spectral changes of the redox-active species of ferrocenyl-

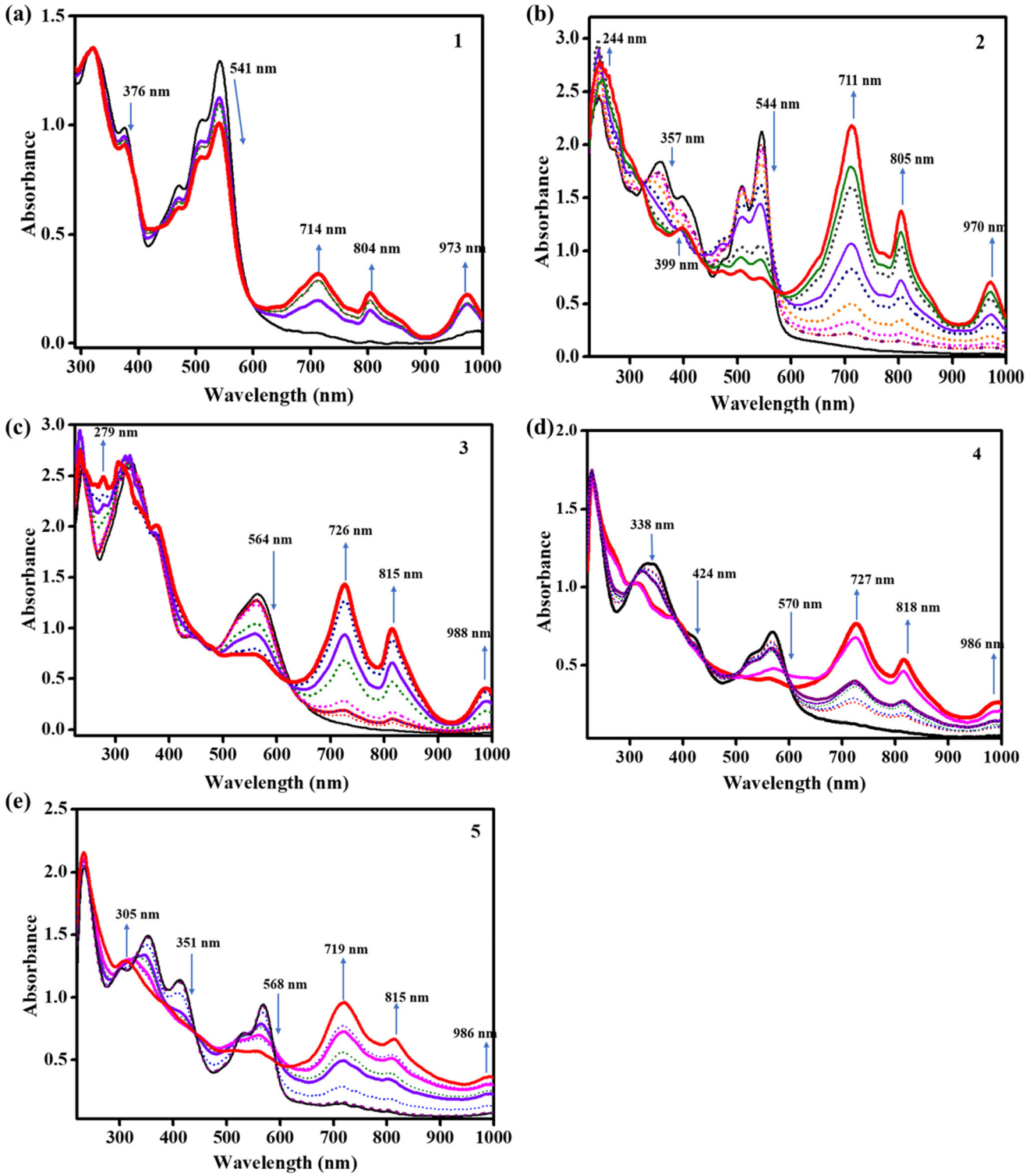

Fig. 4 Stepwise reduction of the PDI derivatives **1–5** under spectroelectrochemical conditions in a DCM/0.50 M Bu_4NPF_6 system. Spectroelectrochemical changes observed (a) for **1**, (b) for **2**, (c) for **3**, (d) for **4**, and (e) for **5** in reduction cycles. Initial spectrum: black.

Published on 20 August 2024. Downloaded on 3/15/2026 4:50:25 AM.

functionalized PDI derivatives **1–5** during the applied redox potentials. The experiment was conducted in dry DCM using a 0.5 M Bu_4NPF_6 supporting electrolyte, and the spectral changes were recorded and are shown in Fig. 4. The PDI derivatives **1–5** exhibited multi-redox waves in the oxidation and reduction processes (Fig. 3 and S16†). The PDI derivative **1** exhibits two reduction cycles and one oxidation cycle. Upon applying the first reduction cycle, there is progressive evolution of a series of absorption bands at 714, 804, and 973 nm. Further, there was no change in the absorption spectra on applying the second reduction cycle, except for the increase in the peak intensity that was observed during the first reduction cycle (Fig. 4a, solid red line). During the oxidation process, no significant change was observed in the absorption spectrum (Fig. S16a†). Derivative **2** shows four reduction cycles and one oxidation cycle. During the first reduction cycle, the intensities of the absorption bands at 357 and 544 nm decreased, and three new intense absorption bands at 711, 805, and 970 nm were observed (Fig. 4b, solid purple line). Similar absorption spectra with increased peak intensities at 711, 805, and 970 nm were observed in the second reduction cycle (Fig. 4b, solid green line). In the third reduction cycle of the PDI derivative **2**, the absorption bands at 357 and 544 nm disappeared. Additionally, a new peak at 399 nm was observed and the peaks at 711, 805, and 970 nm intensified (Fig. 4b, solid red line). In the fourth reduction cycle, the same results were obtained as those observed in the third reduction cycle (Fig. 4b, solid red line). No response was observed during the oxidation cycle for derivative **2**, and the absorption spectra remain unchanged (Fig. S16b†). The PDI derivative **3** showed two reduction potential waves due to PDI and one oxidation potential wave due to ferrocene. The first reduction cycle resulted in a decrease in the intensity of the absorption band at 564 nm and the appearance of three new intense bands at 726, 815, and 988 nm (Fig. 4c, solid purple line). During the second reduction cycle, a new absorption band was observed at 279 nm and a decrease in the intensity of the absorption band at 564 nm was observed while an increase in the intensities of absorbance bands at 726, 815, and 988 nm was observed (Fig. 4c, solid red line). During the oxidation cycle, a new absorption band at 333 nm was observed and the peak at 326 nm disappeared (Fig. S16c†).

In the case of the first reduction cycle of derivative **4**, we observed a decrease in the intensities of absorption bands at 338, 424, and 570, nm and three new absorption bands appeared at 727, 818, and 986 nm (Fig. 4d, solid purple line). No change in the peaks was observed during the second reduction cycle (Fig. 4d, solid purple line). The absorption bands at 338, 424, and 570 nm vanished while the peaks at 727, 818, and 986 nm were more intensified during the third and fourth reduction cycles (Fig. 4d, solid red line). No noticeable difference was observed in the oxidation cycle (Fig. S16d†). During the first reduction cycle of derivative **5**, the intensities of absorption bands at 351 and 568 nm reduced and three new bands at 719, 815, and 986 nm were observed (Fig. 4e, solid purple line). The same results were

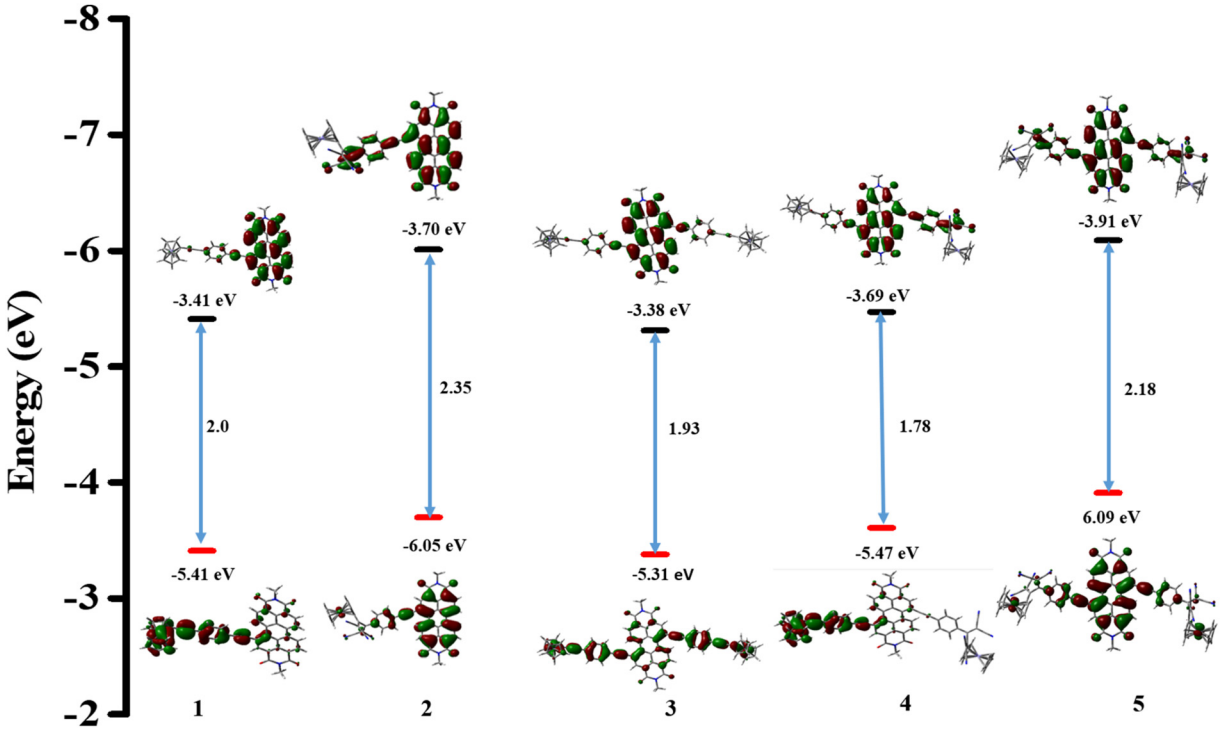

Fig. 5 Frontier molecular orbitals and optimized geometries of the donor–acceptor PDI derivatives **1–5** estimated by DFT calculations using B3LYP/6-31G(d,p)/Lanl2DZ.

 This journal is © The Royal Society of Chemistry 2024

Published on 20 August 2024. Downloaded on 3/15/2026 4:50:25 AM.

found for the second reduction cycle, while during the third reduction cycle, the absorption bands at 351 and 568 nm disappeared, a new absorption band at 305 nm appeared, and the absorption bands at 719, 815, and 986 nm were intensified (Fig. 4e, solid red line). No significant change was observed in the fourth reduction cycle. In the case of the oxidation cycle of compound **5**, no significant change was observed in the absorption spectra (Fig. S16e†).

Theoretical studies

The computational study was performed using the Gaussian 09W program with the B3LYP functional and the 6-31G(d,p) basis set for C, H, O, and N atoms and the Lanl2DZ set for Fe.[58] The study examined the geometries and electronic properties of the ferrocenyl PDI-based donor–acceptor chromophores **1–5**. To make calculations easier, the N–C_8 chain on PDI was replaced by the NC_1 (methyl) group. Fig. 5 depicts the optimized geometry and the estimated highest occupied molecular orbitals (HOMOs) and lowest unoccupied molecular orbitals (LUMOs) for chromophores **1–5**.

The donor–acceptor compounds **1–5** containing ferrocenyl-functionalized perylenediimide possess a non-planar geometry due to the twisted backbone of the perylenediimide unit. In the optimized geometry of derivative **1**, it can be observed that the densities of HOMOs are concentrated on the donor ferrocenyl moiety, while the densities of LUMOs are concentrated on the PDI moiety with some coefficients on the phenyl bridge. On the other hand, in the case of the PDI derivative **2**, the HOMOs are spread over both the PDI and ferrocenyl units, while the LUMOs are delocalized over the acceptor TCBD and PDI moieties. In derivative **3**, the LUMOs are mainly localized on the PDI moiety, while the HOMOs are primarily localized on the ferrocenyl units and some coefficients on the PDI central core. For the unsymmetrical TCBD-substituted PDI

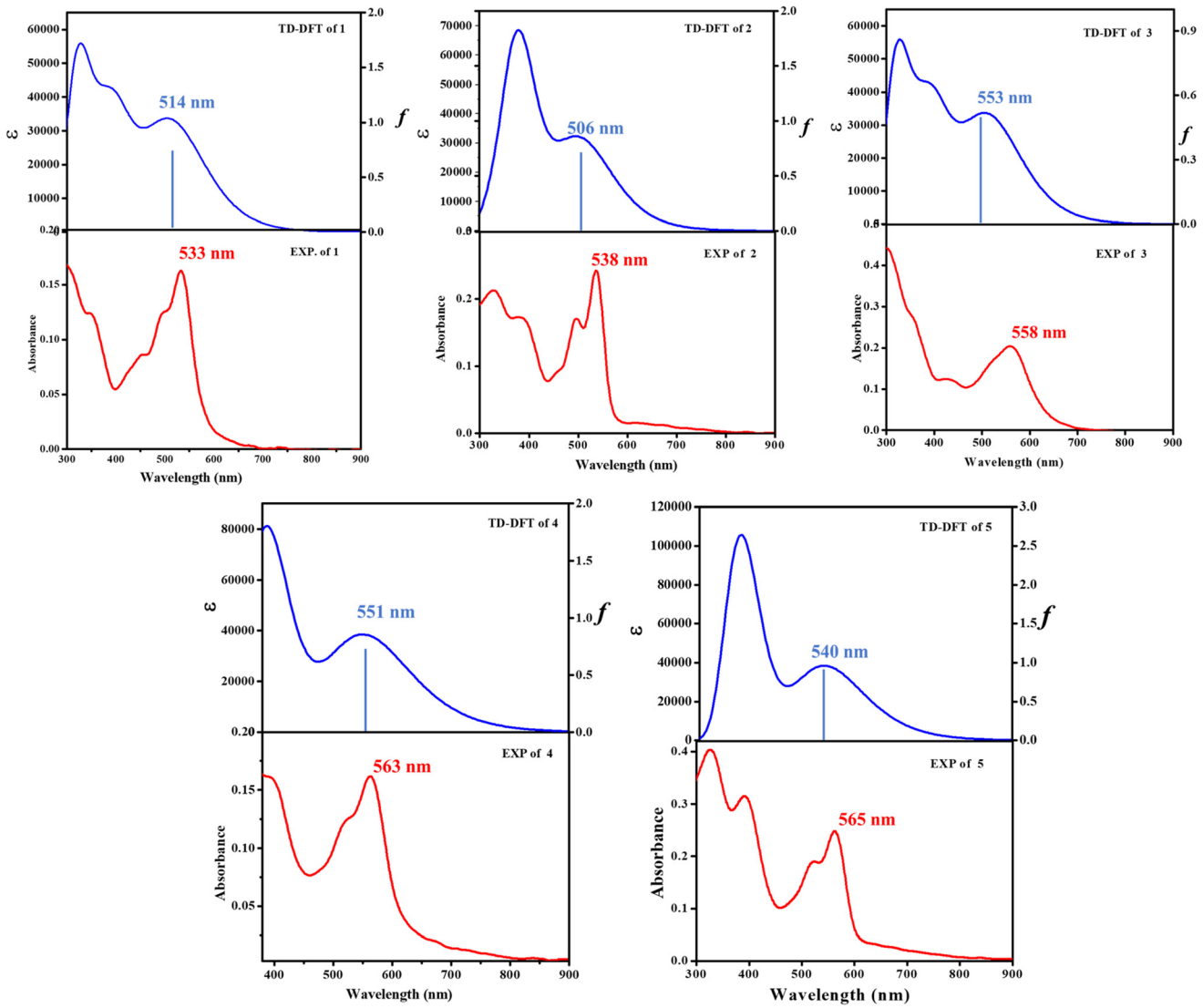

Fig. 6 UV-vis absorption spectra of the push–pull chromophores **PDI 1–5**. Experimental (bottom) and TD-DFT-predicted (top) in DCM solvent.

Published on 20 August 2024. Downloaded on 3/15/2026 4:50:25 AM.

derivative **4**, the HOMOs are located primarily on the ferrocenyl moiety and the phenyl bridge, whereas the LUMOs are located on the PDI–TCBD unit. In the PDI derivative **5**, the HOMOs are widely distributed throughout the molecule, whereas the LUMOs are primarily delocalized over the PDI–TCBD unit. According to these results, the electron density in the LUMOs is distributed over the acceptor PDI–TCBD unit, whereas the HOMOs are located on the donor ferrocene moiety in derivatives **1–5**. The computationally calculated HOMO and LUMO energy levels and the corresponding energy gap are shown in Fig. 5. The theoretically computed energy gap follows the trend of the experimental results (CV and UV), which is **2** > **1** > **5** > **3** > **4**.

The electronic transitions, absorption spectra, oscillator strengths, and extinction coefficients of PDI chromophores **1–5** were computed using time-dependent density functional theory (TD-DFT) at the CAM-B3LYP/6-31G(d,p) level. The data presented in Fig. 6 and Table 2 indicate good agreement between the experimental and theoretical absorption spectra of all the chromophores.

The observed transitions are attributed to π–π* interactions, originating from the HOMO → LUMO transitions of the perylenediimide core. The electronic absorption wavelengths calculated theoretically are slightly lower than the experimental values; this may be due to the temperature, dipole moments, and solvent effects.

The electrostatic potentials (ESPs) of PDI derivatives **1–5**, studied using B3LYP/6-31G(d,p), are shown in Fig. S9.† The ESP map uses colors to indicate charge density localized over ferrocene and PDI: red for high negative potential, blue for high positive potential, and green for neutral. High electron density areas (red zones) are chemically reactive. The negative charge density is localized over the oxygen and cyano groups, while the positive potential is on the ferrocenyl unit. The electron density delocalizes from the ferrocenyl donor to the PDI–TCBD acceptor. The density of states (DOS) is used to study the HOMO–LUMO energy levels and electron density in molecules. The DOS shows contributions of HOMO and LUMO orbitals and energy states for current transitions. Fig. S20† displays the DOS spectra of PDI compounds **1–5** with energy levels on the abscissa and relative strength on the ordinate. The spectra are divided into total (black), acceptor (blue), and donor (magenta and green) parts. The HOMO and LUMO are primarily from the acceptor with the HOMO–LUMO energy gap calculated using CV studies.[56,57]

Table 2 Calculated electronic transition of compounds PDI **1–5**

Compounds	Wavelength	Composition	f^a	Assignment
1	514	HOMO → LUMO (0.63)	0.76	π–π*
2	506	HOMO → LUMO (0.68)	0.74	π–π
3	553	HOMO → LUMO (0.57)	0.66	π–π*
4	551	HOMO → LUMO (0.58)	0.77	π–π*
5	540	HOMO → LUMO (0.69)	0.92	π–π*

[a] *f* oscillator strengths.

Conclusion

In this manuscript, we report the synthesis and characterization of five donor–acceptor derivatives based on perylenediimide, ferrocene as the peripheral group, and TCBD as a strong electron acceptor. A bathochromic shift was observed in the absorption spectra when the number of ferrocenyl and TCBD groups varied at the bay position of PDI. The thermogravimetric analysis (TGA) of the donor–acceptor PDI derivatives **1–5** shows that the TCBD-substituted derivative **3** exhibits the highest thermal stability as compared to other derivatives. The electrochemical analysis revealed that the delocalization of the electron density from ferrocene to the acceptor PDI–TCBD moiety results in anodic shifts as compared to the unsubstituted ferrocene. The spectroelectrochemical investigation of the ferrocenyl-functionalized PDI derivatives **1–5** revealed their NIR electronic absorption spectra in the range of 700–1000 nm on applying a reduction potential. While applying the oxidation cycle, no significant response was observed.

Experimental section

General methods

All the moisture and oxygen-sensitive reactions were performed under an inert atmosphere using the standard inert atmosphere method. ^{1}H NMR spectra were recorded on a Bruker Avance (III) 400 MHz/500 MHz and ^{13}C{^{1}H} NMR spectra were recorded at 100 MHz/125 MHz using $CDCl_3$ as the internal solvent. The ^{1}H NMR chemical shifts were recorded in parts per million (ppm) relative to the solvent residual peak ($CDCl_3$, 7.26 ppm). The ^{13}C{^{1}H} NMR shifts are reported relative to the solvent residual peak ($CDCl_3$, 77.16 ppm). The multiplicities are given as s (singlet), d (doublet), t (triplet), q (quartet), m (multiple), and br. s. (broad singlet) and the coupling constant values (*J*) are reported in Hz. Spectroelectrochemical measurements were performed using a commercially available platinum honeycomb working electrode on a ceramic support, a Pt wire counter electrode, and Ag/AgCl as a reference electrode. The potential was controlled and switched with a potentiostat. The resulting spectroscopic changes were measured using an ALS SEC 2020 spectrometer system. Thermogravimetric analysis was performed using a Mettler Toledo thermal analysis system. The UV-visible absorption spectra of all compounds were recorded using a PerkinElmer LAMBDA 35 UV-visible spectrophotometer in DCM solvent at room temperature. Cyclic voltammograms (CVs) and differential pulse voltammograms (DPVs) were recorded on a PalmSens 4 electrochemical analyzer using glassy carbon as a working electrode, a Pt wire as the counter electrode, and Ag/AgCl as the reference electrode. The scan rate was 50 mV s^{-1} for cyclic voltammetry. A solution of (TBA)ClO_4 in CH_2Cl_2 (0.1 M) was used as the supporting electrolyte.

Synthesis of compound 1

To a degassed solution of mono-bromo-PDI (155 mg, 0.23 mmol), the ferrocenyl precursor (Fc-Ph) (104 mg,

 This journal is © The Royal Society of Chemistry 2024

Published on 20 August 2024. Downloaded on 3/15/2026 4:50:25 AM.

0.34 mmol) in toluene (15 mL), and diisopropylamine (15 mL), $Pd(PPh_3)_4$ (30 mg), and CuI (2 mg) were added. The mixture was heated at 80 °C for 7 h under a N_2 atmosphere. The solvent was removed under reduced pressure and the residue was purified by column chromatography on silica gel eluting with DCM/hexane (80 : 20) to afford **1** as a dark-brown solid (170 mg, 83%). **^{1}H NMR** (500 MHz, $CDCl_3$) δ = 9.97 (d, J = 8.1 Hz, 1 H), 8.54 (d, J = 7.9 Hz, 1 H), 8.50–8.47 (m, 2 H), 8.45 (d, J = 7.9 Hz, 1 H), 8.39 (d, J = 5.3 Hz, 1 H), 8.37 (br. s., 1 H), 7.59–7.55 (d, J = 7.9 Hz, 2 H), 7.54–7.49 (d, J = 7.9 Hz, 2 H), 4.59 (s, 2 H), 4.32 (br. s., 2 H), 4.31 (s, 5 H), 4.16–4.02 (m, 4 H), 1.98–1.90 (m, 2 H), 1.46–1.39 (m, 8 H), 1.36–1.30 (m, 8 H), 1.00–0.95 (m, 6 H), 0.91 (t, J = 6.6 Hz, 6 H), **^{13}C{^{1}H} NMR** (125 MHz, $CDCl_3$) δ: 163.4, 163.2, 163.0, 162.6, 133.6, 133.1, 132.8, 131.7, 131.1, 129.6, 128.4, 127.7, 126.4, 125.9, 123.1, 123.1, 122.6, 121.7, 120.5, 119.5, 100.6, 92.6, 92.4, 85.5, 71.0, 71.0, 70.9, 70.1, 69.3, 69.3, 69.2, 68.4, 38.6, 37.4, 30.8, 28.8, 24.1, 23.1, 22.9, 22.0, 14.6, 13.8, 11.1, 10.2. **HRMS (MALDI-TOF)**: calcd for $C_{60}H_{54}FeN_2O_4$: 922.343, found: 922.265.

Synthesis of compound 2

To a solution of compound **1** (80 mg, 0.086 mmol) in DCM, TCNE (13 mg, 0.095 mmol) was added at rt. The reaction mixture was stirred for 6 h at rt. The solvent was removed under reduced pressure and the residue was purified by column chromatography on silica gel eluting with DCM/hexane (90 : 10) to afford **2** as a dark-brown solid (90 mg, 77%). **^{1}H NMR** (500 MHz, $CDCl_3$) δ: 9.89 (d, J = 8.2 Hz, 1 H), 8.65 (s, 1 H), 8.56 (d, J = 7.9 Hz, 1 H), 8.54–8.49 (m, J = 7.8 Hz, 2 H), 8.47–8.43 (m, J = 8.1 Hz, 2 H), 7.79–7.77 (d, 2 H), 7.75–7.73 (d, 2 H), 5.45 (m, 1 H), 5.03 (m, 1 H), 4.87 (m, 1 H), 4.52 (m, 1 H), 4.43 (s, 5 H), 4.11–4.03 (m, 4 H), 1.91–1.85 (m, 2 H), 1.36–1.32 (m, 8 H), 1.26 (m, 8 H), 0.91–0.87 (m, 6 H), 0.84–0.81 (m, 6 H). **^{13}C{^{1}H} NMR** (125 MHz, $CDCl_3$) δ: 172.0, 165.1, 163.3, 163.1, 163.0, 162.6, 137.9, 134.1, 133.8, 133.3, 133.0, 132.8, 132.0, 131.0, 130.6, 130.3, 129.3, 128.5, 128.2, 127.7, 126.5, 126.4, 125.9, 123.5, 123.3, 123.2, 122.9, 122.7, 122.0, 118.4, 113.6, 113.1, 111.7, 111.6, 97.7, 95.2, 87.2, 78.8, 75.4, 74.8, 72.9, 71.5, 44.3, 38.0, 37.9, 30.8, 29.7, 28.7, 24.1, 23.1, 23.1, 14.2, 14.1, 10.6, 10.6. **HRMS (MALDI-TOF)**: calcd for $C_{66}H_{54}FeN_6O_4$: 1050.356, found: 1050.334.

Synthesis of compound 3

To a degassed solution of di-bromo-PDI (200 mg, 0.26 mmol), the ferrocenyl precursor (Fc-Ph) (200 mg, 0.65 mmol) in toluene (15 mL), and DIPA (15 mL), $Pd(PPh_3)_4$ (40 mg), and CuI (3 mg) were added under a N_2 atmosphere. The mixture was heated at 80 °C for 7 h under a N_2 atmosphere. The solvent was removed under reduced pressure and the residue was purified by column chromatography on silica gel eluting with DCM/hexane (50 : 50) to afford **3** as a dark-brown solid (225 mg, 63%). **^{1}H NMR** (500 MHz, $CDCl_3$) δ: 9.99–9.89 (m, 2 H), 8.74–8.64 (m, 2 H), 8.61–8.53 (m, J = 8.2 Hz, 2 H), 7.61–7.53 (m, 8 H), 4.60 (s, 4 H), 4.31 (s, 4H), 4.29 (s, 10 H), 4.21–4.12 (m, 4 H), 2.02–1.95 (m, 2 H), 1.45 (dd, J = 6.4, 13.4 Hz, 8 H), 1.41–1.36 (m, 8 H), 1.00 (t, J = 7.4 Hz, 6 H), 0.94 (t, J = 6.9 Hz, 6 H). **^{13}C{^{1}H} NMR** (125 MHz, $CDCl_3$) δ: 163.2, 162.9, 137.4, 135.2, 133.5, 133.0, 131.7, 131.7, 130.4, 130.0, 127.9, 127.2, 127.0, 125.6, 122.8, 121.8, 120.8, 119.7, 99.2, 92.4, 92.3, 85.6, 71.7, 70.1, 69.2, 64.7, 44.3, 38.0, 30.9, 28.8, 24.1, 23.1, 14.2, 10.6. **HRMS (MALDI-TOF)**: calcd for $C_{80}H_{66}Fe_2N_2O_4$: 1230.37, found: 1230.253.

Synthesis of compound 4

To the solution of compound **3** (80 mg, 0.065 mmol) in DCM, TCNE (9 mg,0.065 mmol) was added at rt. The reaction mixture was stirred for 6 h at rt. The solvent was removed under reduced pressure and the residue was purified by column chromatography on silica gel eluting with DCM to afford **4** as a black solid (30 mg, 37%). **^{1}H NMR** (500 MHz, $CDCl_3$) δ = 9.91 (d, J = 8.1 Hz, 1 H), 9.76 (d, J = 8.1 Hz, 1 H), 8.74 (s, 1 H), 8.68 (s, 1 H), 8.57 (d, J = 8.4 Hz, 1 H), 8.54 (d, J = 8.4 Hz, 1 H), 7.74–7.67 (m, 4 H), 7.56–7.49 (m, 4 H), 5.54 (br. s., 1 H), 5.10 (br. s., 1 H), 4.94 (br. s., 1 H), 4.60 (s, 2 H), 4.56 (br. s., 1 H), 4.49 (s, 5 H), 4.33 (s, 2 H), 4.31 (s, 5 H), 4.23–4.06 (m, 4 H), 2.00–1.90 (m, 2 H), 1.41 (dd, J = 6.7, 14.0 Hz, 8 H), 1.34 (br. s., 8 H), 0.97 (t, J = 6.8 Hz, 6 H), 0.91 (br. s., 6 H). **^{13}C{^{1}H} NMR** (125 MHz, $CDCl_3$) δ: 172.0, 165.0, 163.2, 163.2, 162.9, 137.5, 137.4, 134.3, 133.8, 133.3, 132.9, 132.8, 131.7, 131.7, 130.0, 129.1, 128.9, 127.9, 127.8, 127.3, 127.3, 127.1, 125.8, 123.3, 122.9, 122.1, 122.1, 120.6, 120.2, 118.5, 113.6, 113.0, 111.6, 99.1, 96.1, 95.3, 92.6, 92.3, 86.8, 85.5, 78.8, 75.2, 74.7, 72.9, 71.7, 71.3, 70.1, 69.3, 64.6, 44.4, 38.0, 30.8, 28.8, 24.1, 23.1, 14.2, 10.6., **HRMS (MALDI-TOF)**: calcd for $C_{86}H_{66}Fe_2N_6O_4$: 1358.384, found: 1358.333.

Synthesis of compound 5

To the solution of compound **3** (50 mg, 0.041 mmol) in DCM, TCNE (13 mg, 0.102 mmol) was added at rt. The reaction mixture was stirred for 6 h at rt. The solvent was removed under reduced pressure and the residue was purified by column chromatography on silica gel eluting with DCM/EtOAc (95 : 5) to afford **5** as a dark-brown solid (55 mg, 90%). **^{1}H NMR** (500 MHz, $CDCl_3$) δ: 9.84 (d, J = 8.1 Hz, 2 H), 8.90–8.73 (m, 2 H), 8.62 (d, J = 8.1 Hz, 2 H), 7.73 (s, 8 H), 5.53 (m, 2 H), 5.13–5.08 (m, 2 H), 4.94 (m, 2 H), 4.57 (m, 2 H), 4.50 (s, 10 H), 4.17 (dd, J = 7.5, 15.4 Hz, 4 H), 1.96 (m, 2 H), 1.45–1.39 (m, 8 H), 1.36–1.31 (m, 8 H), 1.02–0.94 (m, 6 H), 0.94–0.89 (m, 6 H). **^{13}C{^{1}H} NMR** (125 MHz, $CDCl_3$) δ: 172.0, 165.0, 163.5, 138.0, 137.6, 132.8, 131.9, 130.7, 129.6, 129.2, 127.8, 127.3, 123.8, 123.3, 122.4, 121.9, 118.9, 113.6, 113.0, 111.5, 95.1, 87.1, 78.7, 76.7, 76.3, 75.3, 74.7, 72.9, 72.5, 71.3, 44.5, 38.0, 30.8, 29.7, 28.7, 24.1, 23.1, 14.2, 10.6., **HRMS (MALDI-TOF)**: calcd for $C_{92}H_{66}Fe_2N_{10}O_4$: 1486.397, found: (M + H) 1487.329.

Data availability

The experimental details, UV-visible spectra, the TGA study, CV analysis, DFT and TD-DFT calculations, and the spectro-electrochemical study are presented in the manuscript. ^{1}H

Published on 20 August 2024. Downloaded on 3/15/2026 4:50:25 AM.

NMR, ^{13}C NMR, HRMS (MALDI-TOF), the solvatochromic study, DPVs, MEP, the TDOS spectrum, and the cartesian coordinates of DFT and TD-DFT are available in the ESI.†

Conflicts of interest

There are no conflicts to declare.

Acknowledgements

We acknowledge the support from the Council of Scientific and Industrial Research (Project No. 01/3112/23/EMR-II) and the Science and Engineering Research Board (SERB) projects CRG/2022/000023 and STR/2022/000001, New Delhi. We are grateful to the DST-FIST for a grant for the 500 MHz NMR facility and the Sophisticated Instrumentation Centre (SIC), Indian Institute of Technology (IIT) Indore. M. W. thanks the Indian Institute of Technology Indore for the fellowship.

References

1 Y. Jiao, S. Liu, Z. Shen, L. Mao, Y. Ding, D. Ren, F. T. Eickemeyer, L. Pfeifer, D. Cao, W. Xu, J. Song, B. Mi, Z. Gao, S. M. Zakeeruddin, W. Huang and M. Grätzel, *J. Mater. Chem. A*, 2021, **9**, 26311–26322.
2 M. Poddar, Y. Jang, R. Misra and F. D'Souza, *Chem. – Eur. J.*, 2020, **26**, 6869–6878.
3 R. K. Konidena, K. R. J. Thomas, S. Kumar, Y.-C. Wang, C.-J. Li and J.-H. Jou, *J. Org. Chem.*, 2015, **80**, 5812–5823.
4 S. Revoju, A. Matuhina, L. Canil, H. Salonen, A. Hiltunen, A. Abate and P. Vivo, *J. Mater. Chem. C*, 2020, **8**, 15486–15506.
5 P. Srinivasa Rao, S. Brixi, D. B. Shaikh, M. Al Kobaisi, B. H. Lessard, S. V. Bhosale and S. V. Bhosale, *Eur. J. Org. Chem.*, 2021, 2615–2624.
6 K. Erden and C. Dengiz, *J. Org. Chem.*, 2022, **87**, 4385–4399.
7 Y. Jang, Y. Rout, R. Misra and F. D'Souza, *J. Phys. Chem. B*, 2021, **125**, 4067–4075.
8 M. Poddar, A. Cesaretti, E. Ferraguzzi, B. Carlotti and R. Misra, *J. Phys. Chem. C*, 2020, **124**, 17864–17878.
9 A. Nowak-Król and F. Würthner, *Org. Chem. Front.*, 2019, **6**, 1272–1318.
10 R. Roy, A. Khan, O. Chatterjee, S. Bhunia and A. L. Koner, *Org. Mater.*, 2021, **3**, 417–454.
11 T. Weil, T. Vosch, J. Hofkens, K. Peneva and K. Müllen, *Angew. Chem., Int. Ed.*, 2010, **49**, 9068–9093.
12 O. Krupka and P. Hudhomme, *Int. J. Mol. Sci.*, 2023, **24**, 6308.
13 H. Wang, L. Chen and Y. Xiao, *J. Mater. Chem. C*, 2019, **7**, 835–842.
14 M. R. Biradar, S. V. Bhosale, P. P. Morajakar and S. V. Bhosale, *Fuel*, 2022, **310**, 122487.
15 X. Zhan, A. Facchetti, S. Barlow, T. J. Marks, M. A. Ratner, M. R. Wasielewski and S. R. Marder, *Adv. Mater.*, 2011, **23**, 268–284.
16 N. Liang, D. Meng and Z. Wang, *Acc. Chem. Res.*, 2021, **54**, 961–975.
17 M. E. Farahat and G. C. Welch, *Colorants*, 2023, **2**, 151–178.
18 F. Würthner, C. R. Saha-Möller, B. Fimmel, S. Ogi, P. Leowanawat and D. Schmidt, *Chem. Rev.*, 2016, **116**, 962–1052.
19 C. Popli, R. Misra and H. Butenschön, *J. Organomet. Chem.*, 2024, **1006**, 122998.
20 Y. H. Zhou, Z. F. Yang, W. C. Wu, H. J. Xia, S. P. Wen and W. J. Tian, *Chin. Phys.*, 2007, **16**, 2136.
21 J. Li, F. Dierschke, J. Wu, A. C. Grimsdale and K. Mullen, *J. Mater. Chem.*, 2006, **16**, 96.
22 T. Guner, E. Aksoy, M. M. Demir and C. Varlikli, *Dyes Pigm.*, 2019, **160**, 501–508.
23 M. Poddar and R. Misra, *Chem. – Asian J.*, 2017, **12**, 2908–2915.
24 M. L. H. Green, S. R. Marder, M. E. Thompson, J. A. Bandy, D. Bloor, P. V. Kolinsky and R. J. Jones, *Nature*, 1987, **330**, 360.
25 P. Gautam, B. Dhokale, V. Shukla, C. P. Singh, K. S. Bindra and R. Misra, *J. Photochem. Photobiol., A*, 2012, **239**, 24–27.
26 M. Sailer, F. Rominger and T. J. J. Müller, *J. Organomet. Chem.*, 2006, **691**, 299–308.
27 Y. Patil, H. Butenschön and R. Misra, *Chem. Rec.*, 2023, **23**, e202200208; T. Michinobu, C. Boudon, J.-P. Gisselbrecht, P. Seiler, B. Frank, N. N. P. Moonen, M. Gross and F. Diederich, *Chem. – Eur. J.*, 2006, **12**, 1889–1905.
28 C. Philippe, A. T. Bui, M. Beau, H. Bloux, F. Riobé, O. Mongin, T. Roisnel, M. Cordier, F. Paul, L. Lemiègre and Y. Trolez, *Chem. – Eur. J.*, 2022, **28**, e202200025.
29 C. Philippe, A. T. Bui, S. Batsongo-Boulingui, Z. Pokladek, K. Matczyszyn, O. Mongin, L. Lemiègre, F. Paul, T. A. Hamlin and Y. Trolez, *Org. Lett.*, 2021, **23**, 2007–2012.
30 C. Philippe, J. Melan, A. Barsella, T. Vives, Y. R. Leroux, F. R. Guen, L. Lemiègre, D. Jacquemin, S. Gauthier and Y. Trolez, *Tetrahedron Chem*, 2023, **5**, 100036.
31 A. H. Dar, V. Gowri, A. Gopal, A. Muthukrishnan, A. Bajaj, S. Sartaliya, A. Selim, Md. E. Ali and G. Jayamurugan, *J. Org. Chem.*, 2019, **84**, 8941–8947.
32 K. M. Neethu, K. Nag, A. H. Dar, A. Bajaj, S. A. Gopal, V. Gowri, M. Nagpure, S. Sartaliya, R. Sharma, A. K. Solanki, M. E. Ali, A. Muthukrishnan and G. Jayamurugan, *Org. Biomol. Chem.*, 2023, **21**, 2922–2929.
33 K. Erden and C. Dengiz, *J. Org. Chem.*, 2022, **87**, 4385–4399.
34 I. S. Yadav and R. Misra, *New J. Chem.*, 2022, **46**, 15999–16006.
35 Y. Patil, C. Popli and R. Misra, *New J. Chem.*, 2018, **42**, 3892–3899.
36 S. Huang, J. Ma, Y. Yi, M. Li, P. Cai and N. Wu, *Org. Biomol. Chem.*, 2022, **20**, 4081–4085.
37 T. Michinobu, *J. Am. Chem. Soc.*, 2008, **130**, 14074–14075.
38 (*a*) F. Khan, Y. Jang, Y. Patil, R. Misra and F. D'Souza, *Angew. Chem., Int. Ed.*, 2021, **133**, 20681–20690; (*b*) N. Ripoche, M. Betou, C. Philippe, Y. Trolez, O. Mongin, M. Dudek, Z. Pokladek, K. Matczyszyn, M. Samoc,

 This journal is © The Royal Society of Chemistry 2024

Published on 20 August 2024. Downloaded on 3/15/2026 4:50:25 AM.

H. Sahnoune, J.-F. Halet, T. Roisnel, L. Toupet, M. Cordier, G. J. Moxey, M. G. Humphrey and F. Paul, *Phys. Chem. Chem. Phys.*, 2021, **23**, 22283–22297.
39 A. T. Bui, C. Philippe, M. Beau, N. Richy, M. Cordier, T. Roisnel, L. Lemiègre, O. Mongin, F. Paul and Y. Trolez, *Chem. Commun.*, 2020, **56**, 3571–3574.
40 S. Kato, H. Noguchi, S. Jin and Y. Nakamura, *Asian J. Org. Chem.*, 2016, **5**, 246–256.
41 T. Michinobu, J. C. May, J. H. Lim, C. Boudon, J.-P. Gisselbrecht, P. Seiler, M. Gross, I. Biaggio and F. Diederich, *Chem. Commun.*, 2005, 737–739.
42 G. Jayamurugan, J.-P. Gisselbrecht, C. Boudon, F. Schoenebeck, W. B. Schweizer, B. Bernet and F. Diederich, *Chem. Commun.*, 2011, **47**, 4520–4522.
43 T. Shoji, S. Ito, K. Toyota, M. Yasunami and N. Morita, *Chem. – Eur. J.*, 2008, **14**, 8398–8408.
44 S. Kato, T. Kijima, Y. Shiota, T. Abe, S. Kuwako, H. Miyauchi, N. Yoshikawa, K. Yamamoto, K. Yoshizawa, T. Yoshihara, S. Tobita and Y. Nakamura, *Org. Biomol. Chem.*, 2020, **18**, 4198–4209.
45 S. Kato and F. Diederich, *Chem. Commun.*, 2010, **46**, 1994–2006.
46 N. Krause, M. Kielmann, J. Ma and H. Butenschön, *Eur. J. Org. Chem.*, 2015, 2622–2631.
47 B. Dhokale, T. Jadhav, Y. Patil and R. Misra, *Dyes Pigm.*, 2016, **134**, 164–170.
48 B. Dhokale, P. Gautam and R. Misra, *Tetrahedron Lett.*, 2012, **53**, 2352–2354.
49 A. Auger, A. J. Muller and J. C. Swarts, *Dalton Trans.*, 2007, **33**, 3593–3716.
50 M. Sheokand, N. J. Tiwari and R. Misra, *Org. Biomol. Chem.*, 2023, **21**, 3896–3905.
51 Y. Rout, V. Chauhan and R. Misra, *J. Org. Chem.*, 2020, **85**, 4611–4618.
52 D. Nauroozi, C. Bruhn and R. Faust, *Organometallics*, 2019, **38**, 2553–2557.
53 B. Dhokale, T. Jadhav, Y. Patil and R. Misra, *Dyes Pigm.*, 2016, **134**, 164–170.
54 S. Vajiravelu, L. Ramunas, G. J. Vidas, G. Valentas, J. Vygintas and S. Valiyaveettil, *J. Mater. Chem.*, 2009, **19**, 4268.
55 Y. Zhao, X. Li, Z. Wang, W. Yang, K. Chen, J. Zhao and G. G. Gurzadyan, *J. Phys. Chem. C*, 2018, **122**, 3756–3772.
56 H. Baig, A. Iqbal, A. Rasool, S. Z. Hussain, J. Iqbal, M. Alazmi, N. Alshammari, A. Alazmi, A. AlGhadhban, A. M. E. Sulieman, K. B. Said, H. Rehman and R. S. Z. Saleem, *ACS Omega*, 2023, **8**, 28499–28510.
57 A. Sugie, W. Han, N. Shioya, T. Hasegawa and H. Yoshida, *J. Phys. Chem. C*, 2020, **124**, 9765–9773.
58 M. J. Frisch, G. W. Trucks, G. W. Schlegel, G. E. Scuseria, M. A. Robb, J. R. Cheeseman, G. Scalmani, V. Barone, G. A. Petersson, L. X. Nakatsuji, M. Caricato, A. Marenich, J. Bloino, B. G. Janesko, R. Gomperts, B. Mennucci, H. P. Hratchian, J. V. Ortiz, A. F. Izmaylov, J. L. Sonnenberg, D. Williams-Young, F. Ding, F. Lipparini, F. Egidi, J. Goings, B. Peng, A. Petrone, T. Henderson, D. Ranasinghe, V. G. Zakrzewski, J. Gao, N. Rega, G. Zheng, W. Liang, M. Hada, M. Ehara, K. Toyota, R. Fukuda, J. Hasegawa, M. Ishida, T. Nakajima, Y. Honda, O. Kitao, H. Nakai, T. Vreven, K. Throssell, J. A. Montgomery, J. E. Peralta Jr., F. Ogliaro, M. Bearpark, J. J. Heyd, E. Brothers, K. N. Kudin, V. N. Staroverov, T. Keith, R. Kobayashi, J. Normand, K. Raghavachari, A. Rendell, J. C. Burant, S. S. Iyengar, J. Tomasi, M. Cossi, J. M. Millam, M. Klene, C. Adamo, R. Cammi, J. W. Ochterski, R. L. Martin, K. Morokuma, O. Farkas, J. B. Foresman and D. J. Fox, *Gaussian 09, rev. A.02*, Gaussian, Inc., Wallingford, CT, 2016.